Research Article | Vol. 27, No. 11 | 27 May 2019 | OPTICS EXPRESS 15236
Optics EXPRESS

Theoretical study of bicharacteristic waveguide for fundamental-mode phase-matched SHG from MIR to NIR

TIANYE HUANG,[1,2,*] GUIZHEN XU,[1] JIANXING PAN,[1] ZHUO CHENG,[1] PERRY PING SHUM,[3] AND GILBERTO BRAMBILLA[4]

[1]*School of Mechanical Engineering and Electronic Information, China University of Geosciences (Wuhan), Wuhan, China*
[2]*Hubei Key Laboratory of Inland Shipping Technology, Wuhan, China*
[3]*Center of Fiber Technology, Electrical and Electronics Engineering, Nanyang Technological University, Singapore*
[4]*Optoelectronics Research Centre, University of Southampton, Southampton, Hampshire, UK*
**tianye_huang@163.com*

Abstract: In this paper, a bicharacteristic waveguide (BW) is proposed for fundamental-mode phase-matched second harmonic generation (SHG) from mid-infrared (MIR) to near-infrared (NIR). The required phase matching condition (PMC) is satisfied between the fundamental plasmonic mode at 3100 nm and the photonic mode at 1550 nm. With 1 W pump power, the SHG conversion efficiency of 4.173% can be obtained in 90.3 μm length waveguide. Moreover, the SHG conversion can be enhanced by using a microring resonator (MRR). By optimizing the MRR, the SHG conversion efficiency is increased to 8.30%. The proposed waveguide can also provide a promising platform for upconversion detection. By using an on-chip cascaded configuration, a gas sensor with the capability of MIR absorption and NIR detection is proposed. It is found that the detection limit (DL) can reach 1.04 nmol/L with 100 mW pump power, which shows significant enhancement compared with direct MIR absorption and detection.

1. Introduction

Second-order nonlinear optical processes such as second harmonic generation (SHG) have significant applications in various fields e.g. all-optical signal processing [1], wavelength conversion [2], optical switch [3], etc. Benefiting from the planar integrated geometric structure and tight mode profile, optical waveguides provide a potential platform for efficient SHG [4]. Over the last few decades, plasmonic waveguides have attracted great attention in nonlinear photonics due to their extraordinary abilities to break through the traditional optical diffraction limits [5]. Recently, some plasmonic SHG waveguides have been extensively studied, such as the waveguide combined a second-order nonlinear material lithium niobate ($LiNbO_3$) and a plasmonic structure [6–8]. Furthermore, the conversion efficiency can be significantly improved by employing polymer material with much higher second-order nonlinearity [9,10].

Phase matching conditions (PMCs) which ensure the continuous power transfer from pump to harmonic are vital to realize efficient SHG process. Currently, the frequently utilized PMC techniques are based on quasi-phase matching (QPM) or intermodal-phase matching (IMPM) [11–14]. However, the QPM usually relies on the iron exchange technology or grating structure which can complicate the fabrication process. For IMPM, the generated harmonic is in the form of higher-order mode (HOM) which is difficult for post manipulation. Particularly, it is inferior for the application such as photon pair generation since an additional mode convertor is required to produce the target pump mode. Therefore, realizing the PMC between fundamental

#362040 https://doi.org/10.1364/OE.27.015236
Journal © 2019 Received 14 Mar 2019; revised 5 May 2019; accepted 8 May 2019; published 13 May 2019

Optics EXPRESS

modes at both pump and harmonic wavelengths can be a significant step for the waveguide-based SHG devices.

From the point view of operation wavelength, recently, plasmonic waveguides that operate in the mid-infrared (MIR) have received much attention for their wide range of applications such as chemical or gas sensing [15–17]. This is because a large number of molecules' fundamental "fingerprint" frequencies are located in the MIR wavelength region. It is known that the "fingerprint" absorption efficiency is typically more than 100 times stronger than its counterpart in the NIR wavelength region [18]. However, compared to the high performance NIR photodetection, the MIR photodetector usually shows much higher noise and lower sensitivity [19] and therefore limiting the implementation of MIR sensors. To overcome this challenge, upconverting the MIR signal to NIR by using nonlinear parametric process is a potential method [20]. In this scheme, the MIR signal is firstly efficiently absorbed by the "fingerprint" frequency. Then the remaining MIR light is converted to NIR through nonlinear process for detection so that the advantages of high absorption in MIR and efficient detection in NIR are utilized simultaneously. SHG, a parametric process which can connect the frequencies over one octave, can be a potential approach to realize upconversion detection.

As mentioned above, perfect phase matching between fundamental modes and MIR-to-NIR conversion are two challenges for waveguide-based SHG. Recently, transparent conductive oxides (TCOs), such as indium cadmium oxide (CdO) and indium tin oxide (ITO), have attracted important research interests as alternative materials for plasmonics. This is because the dispersion relation can be easily tailored through their carrier concentrations [21,22]. Such property is favorable for constructing optical sensors and modulator [23,24]. It also offers the possibility to support surface plasmon polariton (SPP) in the MIR region where traditional noble metals behave more like perfect conductors. Previous researches on TCO mainly focuses on the metal-like dispersion relation, on the contrary, the dielectric property at the specific wavelength region are not that exploited. The strong dispersion over large wavelength span can offer new opportunities to balance the phase mismatch in SHG process.

In this paper, leveraging on the unique dispersion relation of CdO, a bicharacteristic SHG waveguide with PMC between two fundamental modes is proposed. At MIR, the CdO behaves like metal and supports the plasmonic mode. While at NIR, it becomes a dielectric material and thus a photonic mode can be formed. By optimizing the carrier density and waveguide geometry, these two fundamental modes can be perfectly phase-matched for SHG. Besides the straight waveguide, a microring resonator (MRR) is employed to further enhance the conversion efficiency. Based on this waveguide, we further propose an on-chip gas sensor integrated with the capability of MIR-to-NIR upconversion detection. The results show that the detection limit (DL) of methane can achieve the order of 10^{-9} mol/L which is significantly enhanced comparing to direct MIR detection.

2. SHG in straight waveguide

2.1. Theory and waveguide design

Figure 1(a) shows the plasmonic-photonic bicharacteristic waveguide (BW) structure, where h and w represent the height and width of the proposed waveguide. The polymer considered refers to the one used in [9], and its second order nonlinear susceptibility ($\chi^{(2)}$) is 619.4 pm/V. The refractive indices of the polymer at 3100 nm and 1550 nm are 1.477597 and 1.479017 [25], respectively. The substrate is composed of indium cadmium oxide (CdO), and the entire device is surrounded by the air. According to the Drude model [21], the dielectric constant of CdO is given by

$$\varepsilon = \varepsilon' + j\varepsilon'' = \varepsilon_\infty - \frac{\omega_p}{\omega(\omega + j\gamma)} \tag{1}$$

Optics EXPRESS

$$\omega_p = \sqrt{\frac{ne^2}{m_{eff}\varepsilon_0}} \tag{2}$$

where ε' and ε'' are the real and imaginary parts of the permittivity, respectively. ε_∞ is the high frequency dielectric constant, ω_p is the plasma frequency, ω is the angular frequency of the light wave, γ is the damping degree, n is the electron density, e is the electron charge, ε_0 is the vacuum absolute permittivity, and $m_{eff} = km_0$ is the effective mass of the electron, where m_0 is the mass of the free electron. In this work, $n = 6 \times 10^{26}$ m^{-3}, $e = 1.602 \times 10^{-19}$ C, $\varepsilon_0 = 8.854 \times 10^{-12}$ F/m, $\gamma = 2.92 \times 10^{13}$ rad/s, $m_{eff} = 1.823 \times 10^{-31}$ kg and $\varepsilon_\infty = 5.5$ F/m, respectively.

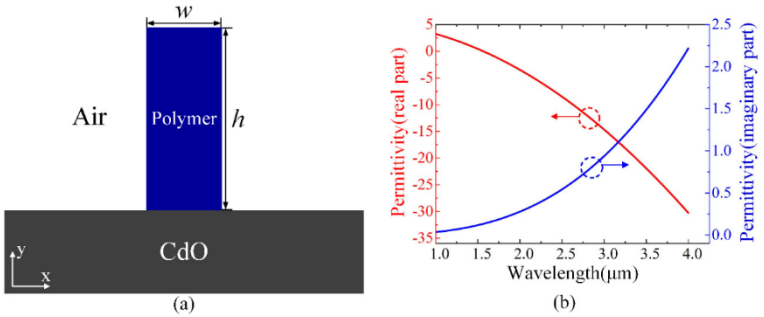

Fig. 1. (a) The cross-section view of the proposed waveguide. (b) CdO permittivity versus wavelength.

The permittivity of CdO is shown in Fig. 1(b). It can be found that the real part of the dielectric constant in NIR is positive. In this case, CdO behaves as dielectric material thus supporting photonic modes. When the wavelength increases to ~1650 nm, the real part of the dielectric constant becomes negative thus supporting plasmonic modes. Here we consider the fundamental TM modes (TM_{00}) of 3100 nm and 1550 nm in the waveguide. The width and height of the BW are optimized to satisfy the PMC for SHG. With the waveguide height h = 2000 nm, the effective mode indices of the fundamental frequency (FF) and the second harmonic frequency (SHF) at different waveguide width are demonstrated in Fig. 2(a). At w = 858 nm, the effective mode indices of FF and SHF are 1.3105 + 0.00685i and 1.3106 + 0.00059i, respectively indicating perfect PMC. The corresponding electric mode profiles of the fundamental modes at 3100 nm and 1550 nm are plotted in Figs. 2(b) and 2(c). At pump wavelength, the fundamental mode demonstrates typical plasmonic nature with strong field near the polymer-CdO interface. On the contrary, at harmonic wavelength, the substrate is dielectric with refractive index smaller than the polymer, therefore total internal reflection is satisfied in the polymer waveguide and consequently fundamental photonic mode is formed. The phase changing property of CdO offers the facilitation for fundamental PMC. It should be mentioned that at 3100 nm, the waveguide only supports fundamental TM mode, thus it is single-mode. At 1550 nm, both the fundamental TM mode and first-order TM mode are supported by the waveguide. However, the phase-mismatch between fundamental TM mode at 3100 nm and first-order TM mode at 1550 nm is as high as 2.1887×10^6 m^{-1}, which will significantly prevent the second harmonic power accumulation. In order to excite the plasmonic mode in the proposed waveguide, the grating coupling methods by satisfying the phase matching condition $k_{SPP} = k_0 \sin\theta + n2\pi/\Lambda$ can be used, where k_{SPP} is the wavevector of surface plasmon mode, k_0 is the wavevector of incident beam, θ is the incident angle, n is integer, Λ is the grating period. The coupling efficiency can be as high as several tens of percent by optimizing the grating parameters [26–28].

Optics EXPRESS

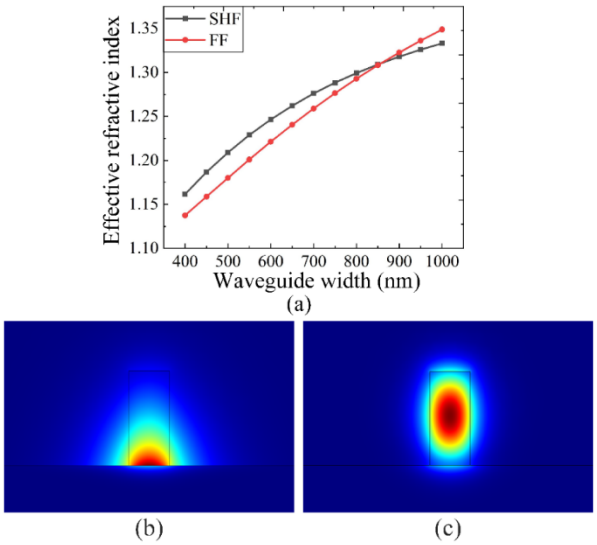

Fig. 2. (a) The effective refractive indices of the plasmonic mode at 3100 nm and photonic mode at 1550 nm with different waveguide widths w at h = 2000 nm. Electric mode profiles of (b) plasmonic mode and (c) photonic mode under PMC.

In addition to PMC, efficient SHG also requires high nonlinear coupling coefficients (NCCs) determined by the nonlinear susceptibility and the mode overlap between the pump and harmonic modes. The definition of the NCC is given in [29]

$$C_X = \varepsilon_0 \iint_{A_{NL}} \chi^{(2)} : \vec{E}_2 \vec{E}_1^* \cdot \vec{E}_1^* \, dxdy \tag{3}$$

where E_1 and E_2 are the electric fields at the modes at 3100 nm and 1550 nm, respectively.

According to our numerical calculation, the NCC of the proposed waveguide is as high as 49.2 $ps \cdot m^{-1} \cdot W^{-1/2}$. It should be noted that different PMCs can be achieved by adjusting the waveguide geometric parameters, as shown in Fig. 3(a). Furthermore, the NCCs can always maintain above 48 $ps \cdot m^{-1} \cdot W^{-1/2}$ with waveguide height from 1600 nm to 2200 nm.

Propagation loss is another important parameter for efficient SHG. The propagation loss α is defined as

$$\alpha = 8.686 k_0 \, \mathrm{Im}[n_{eff}] \tag{4}$$

where $\mathrm{Im}[n_{eff}]$ is the imaginary part of the effective mode index and k_0 is corresponding propagation constant. Figure 3(b) depicts the propagation losses of FF and SHF with different waveguide height under PMCs. With lower waveguide height, the propagation loss of SHF is larger, while the propagation loss of FF is slightly reduced.

Optics EXPRESS

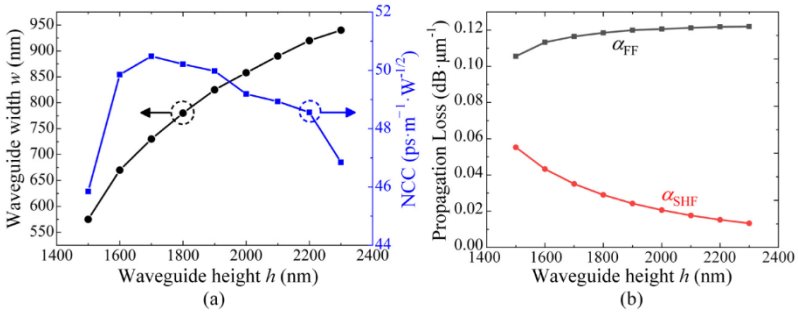

Fig. 3. (a) The waveguide width and corresponding NCC, and (b) the propagation losses of FF and SHF with respect to the waveguide height h under PMCs.

2.2. Performance of SHG in the proposed waveguide

Next, we study the performance of SHG by solving the coupled-mode equations [10]

$$\frac{\partial A_{FF}}{\partial z} = -\frac{1}{2}\alpha_{FF} A_{FF} + i\frac{\omega_{FF}}{4} C_X A_{FF}^{*} A_{SHF} \exp(i\Delta\beta z) \tag{5}$$

$$\frac{\partial A_{SHF}}{\partial z} = -\frac{1}{2}\alpha_{SHF} A_{SHF} + i\frac{\omega_{FF}}{4} C_X^{*} A_{FF} A_{FF} \exp(-i\Delta\beta z) \tag{6}$$

where A_{FF} and A_{SHF} are the slowly varying mode amplitudes of FF and SHF, respectively. α_{FF} and α_{SHF} are the propagation loss coefficients of FF and SHF, and $\Delta\beta$ is the phase mismatch. Under the condition of $h = 2000$ nm and $w = 858$ nm, we calculate $\alpha_{FF} = 0.121$ dB·μm^{-1}, $\alpha_{SHF} = 0.0206$ dB·μm^{-1} and $\Delta\beta = 0$, respectively. We define the SHG conversion efficiency as follow

$$\eta = \frac{P_2(L)}{P_1(0)} \tag{7}$$

where $P_1(0)$ is the input pump power, L is the waveguide length and $P_2(L)$ is the corresponding output SH power.

With 1 W continuous wave (CW) of pump power, the SHG performance is shown in Fig. 4(a). We can find that the SH power reaches a peak of 0.0417 W with the propagation length of 90.3 μm. After the conversion peak, the pump power becomes weak and the nonlinear gain is insufficient to compensate the linear loss of SHF resulting in the decay of conversion with longer waveguide. The peak conversion efficiency and the corresponding waveguide length with different pump power are shown in Fig. 4(b). For a low pump power of 100 mW, the SHG efficiency is still as high as ~0.45%. With pump power of 1 W, SHG conversion efficiencies for different waveguide geometric parameters to satisfy the PMCs are calculated, as shown in Fig. 4(c). When the waveguide height $h = 2200$ nm and the corresponding width $w = 920$ nm, the maximum conversion efficiency of 4.35% can be obtained at 98.3 μm waveguide length. It can be seen that when the waveguide height is from 1.9 μm to 2.3 μm, the conversion efficiency can always reach 4%. In the paper, we use the waveguide with a height of 2 μm to carry out subsequent theoretical analysis. Note that with 7 ns, 10 Hz pulsed laser beam, the damage threshold of commercial polymer sample is measured to be ~20 J/cm^2 [30], corresponding to a peak intensity damage threshold of ~2.9 × 10^8 W/cm^2 in this condition. In practice, the proposed SHG waveguide can operate under such quasi-continuous wave pump as well. According to the effective area of ~0.5 μm^2, with 1 W peak power, the peak power density is ~2 × 10^8 W/cm^2 which is below the damage threshold.

Optics EXPRESS

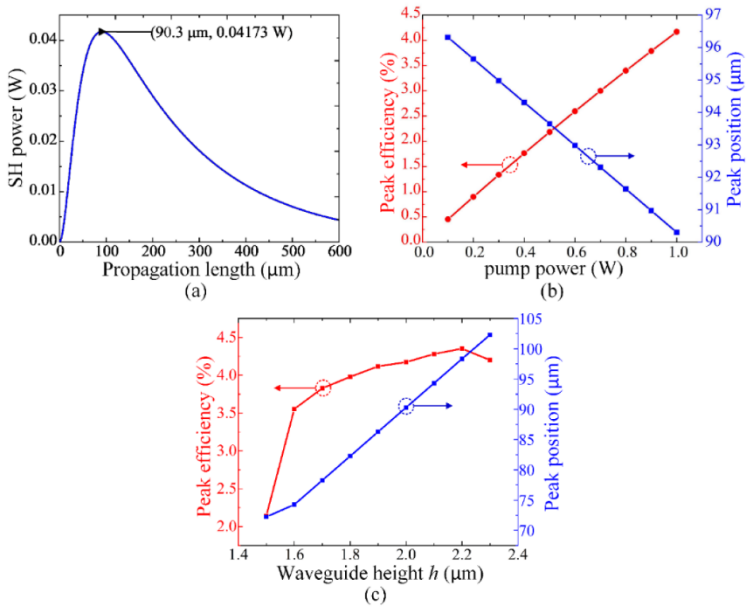

Fig. 4. (a) SH power along propagation length in the waveguide with 1 W pump power. (b) Peak efficiency and the corresponding position under different pump power. (c) Peak efficiency and the corresponding position at different PMC height under 1 W pump.

The fabrication-error can induce degradation to the phase mismatch $\Delta\beta$. Figure 5 depicts the SHG conversion efficiency along propagation length with the different phase mismatch $\Delta\beta$. Considering 3 dB conversion efficiency deviation, the phase mismatch is within the range of $\pm 5.02 \times 10^4$ m^{-1}. Such phase mismatch corresponds to the variation of waveguide height, width and pump wavelength of ± 280 nm, ± 113 nm and ± 125 nm, respectively. Therefore, the proposed waveguide possesses a large fabrication-error tolerance.

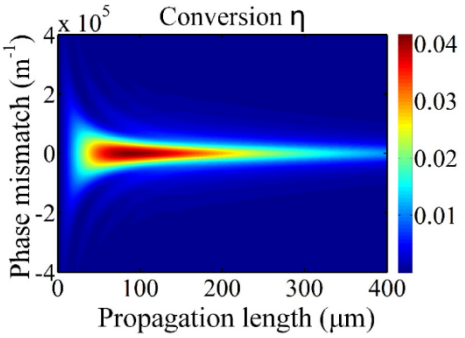

Fig. 5. SHG conversion efficiency along propagation length with different phase mismatch.

3. Enhancement of SHG in microring resonator

3.1. Theory and microring resonator design

To further enhance SHG process, we propose a microring resonator (MRR) based on the proposed waveguide as shown in Figs. 6(a) and 6(b). The pump in the bus waveguide is coupled to the cavity through a coupling gap defined as g. The radius and the width of the ring are R and w_1, respectively.

Optics EXPRESS

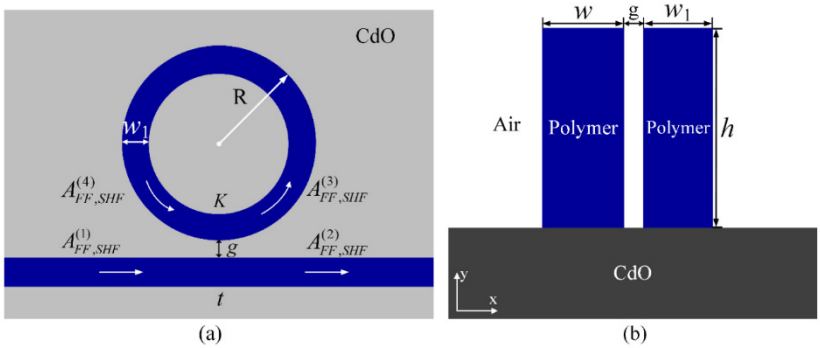

Fig. 6. The cross-section view of the proposed MRR along (a) x-z and (b) x-y planes.

For the bend waveguide, simulations are carried out by using the build-in algorithm in 2D finite difference eigenmode solver (*Mode Solutions from Lumerical*). We readjust the geometric parameters to meet the PMCs, as shown in Fig. 7(a). Furthermore, we obtain the losses of FF and SHF as shown in Fig. 7(b). It should be noted that the loss includes intrinsic loss and bending loss caused by radiation and reflection, so that as the radius decreases, the loss increases exponentially [31]. Therefore, the appropriate parameters should be chosen to get better SHG performance.

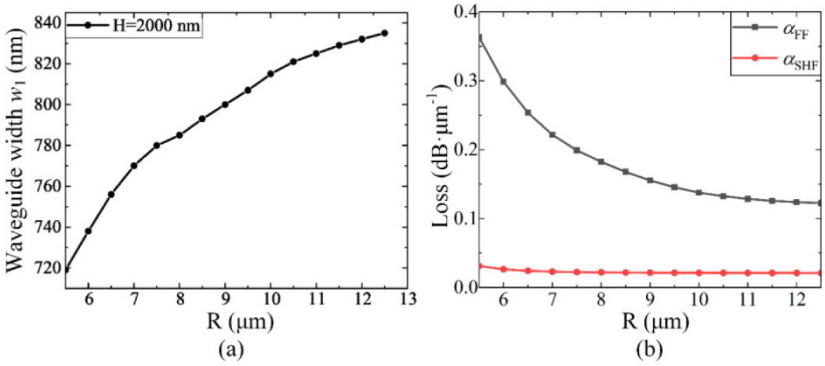

Fig. 7. (a) The bend waveguide width w_1 and (b) the losses of FF and SHF with different radius R under PMCs.

In our work, the resonance condition can be satisfied by choosing the appropriate radius of the ring to enhance the SHG process and the resonance condition for FF and SHF can be defined as follows [32]

$$m_{FF,SHF} = k_{FF,SHF} n_{eff1,2} R \tag{8}$$

where m_{FF} and m_{SHF} known as integers are the azimuth number of resonances at FF and SHF, respectively. n_{eff1} and n_{eff2} are the effective mode indices of FF and SHF, respectively. k_{FF} and k_{SHF} are corresponding propagation constants at FF and SHF. Considering the nearest integer m_{FF}, the radius $R = 9.5$ μm is chosen, corresponding to $m_{FF} = 25$ and $m_{SHF} = 50$, as shown in Fig. 8(a). Under the condition of R = 9.5 μm and w_1 = 807 nm, Figs. 8(b) and 8(c) depict the corresponding electric mode profiles of the fundamental modes at FF and SHF, and the corresponding effective mode indices of FF and SHF are 1.3037 + 0.00827i and 1.3037 + 0.00061i, respectively. The losses of FF and SHF are 0.146 dB·μm^{-1} and 0.0214 dB·μm^{-1}, as shown in Fig. 7(b). Furthermore, we obtain the NCC of the bend waveguide as high as 47.1 ps·m^{-1}·W$^{-1/2}$.

Optics EXPRESS

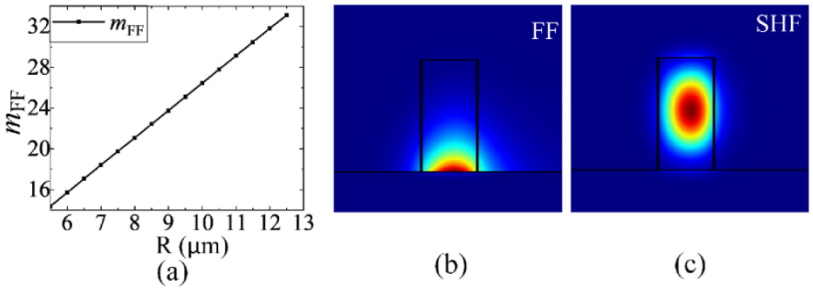

Fig. 8. (a) m_{FF} with different radius R. Electric mode profiles at (b) FF and (c) SHF, when R = 9.5 μm and w_1 = 807 nm.

In the coupling region, as shown in Fig. 6(a), the boundary condition in the MRR can be given by the following equations [32]

$$A_{FF,SHF}^{(2)} = \mathrm{t}_{FF,SHF} A_{FF,SHF}^{(1)} + iK_{FF,SHF} A_{FF,SHF}^{(4)} \tag{9}$$

$$A_{FF,SHF}^{(3)} = iK_{FF,SHF} A_{FF,SHF}^{(1)} + \mathrm{t}_{FF,SHF} A_{FF,SHF}^{(4)} \tag{10}$$

where $A_{FF,SHF}$ are complex mode amplitudes at FF and SHF, and their squared magnitudes correspond to the modal powers, respectively. t and K are the optical field transmission coefficients and coupling coefficients, respectively. Here, K can be calculated by the coupled mode theory [33,34].

With all the other parameters of the MRR determined, the transmission coefficients of t and coupling coefficients of K are only related to the coupling gap distance between the bus waveguide and the ring. Figure 9 demonstrates the transmission coefficients at FF and SHF with respect to different gaps. We can see that t_{SHF} is usually larger than t_{FF}, due to the stronger confinement at shorter wavelength. Then, we calculate the transmission coefficients under the critical coupling conditions of FF (t_{FF}) and SHF (t_{SHF}), respectively. As is shown in Fig. 9, t_{FF} = $\exp(-\pi\alpha_{FF}R)$ = 0.4136 corresponds to the gap of 331 nm, and t_{SHF} = $\exp(-\pi\alpha_{SHF}R)$ = 0.8643 corresponds to the gap of 168 nm. The critical coupling conditions for FF and SHF are different.

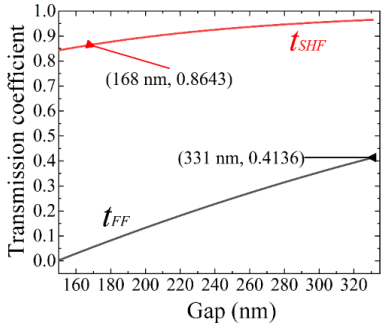

Fig. 9. Transmission coefficients at FF (black line) and SHF (red line) versus different gaps.

3.2. Performance of SHG in the microring resonator

We first choose the gap of g = 168 nm and the corresponding transmission coefficients are t_{FF} = 0.0510 and t_{SHF} = 0.8643, respectively. The SHG performance in the MRR is investigated by solving Eqs. (5) and (6) together with the boundary conditions Eqs. (9) and (10).

With pump power of 100 mW, the output SH power is 1.137 mW corresponding to SHG conversion efficiency of 1.137%, which is more than 2.5 times that in the straight waveguide.

Optics EXPRESS

For the intracavity power, as shown in Fig. 10(a), the SH power reaches a steady value of 3.36 mW after ~44 roundtrips, which means a strong field enhancement in the cavity. The output SH power with respect to different gaps is illustrated in Fig. 10(b). We can see that the maximum SH power in the bus waveguide is 1.216 mW with gap of 210 nm, which is close to the critical coupling condition for SH mode. The conversion at critical coupling condition for FF is 0.833 mW corresponding to g = 331 nm. Therefore, it is better to choose the critical coupling condition for harmonic mode so as to enhance the conversion. It is obvious that the SHG conversion efficiency in the proposed MRR can be enhanced compared to the straight waveguide even with the existence of bending loss.

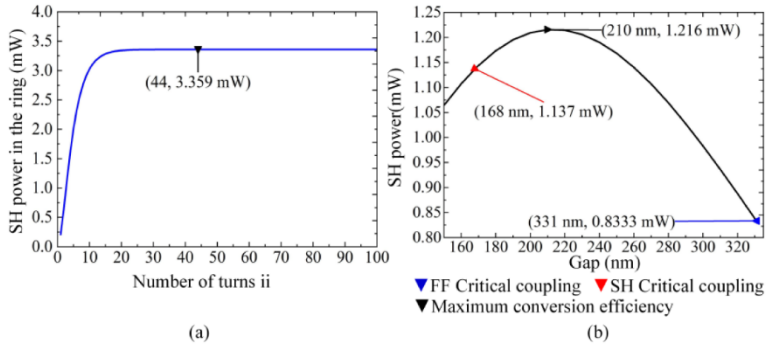

Fig. 10. (a) SH power in the ring versus the number of turns ii. (b) The output SH power with different gaps.

Next, we investigate the output SH power at different pump power with R and g fixed to 9.5 μm and 210 nm, respectively. Both the output SH power and the SHG conversion efficiency are improved with the input pump power increment, as shown in Fig. 11(a). With pump power of 1 W, the output SHG conversion efficiency is calculated to be 8.30%. Figure 11(b) depicts the output SH power and the corresponding optimized gap with different radius of the MRR when the pump power is fixed to 100 mW. It can be seen that the output SH power can reach a maximum value of 1.27 mW at g = 250 nm when R = 11 μm, corresponding to SHG conversion efficiency of 1.27%.

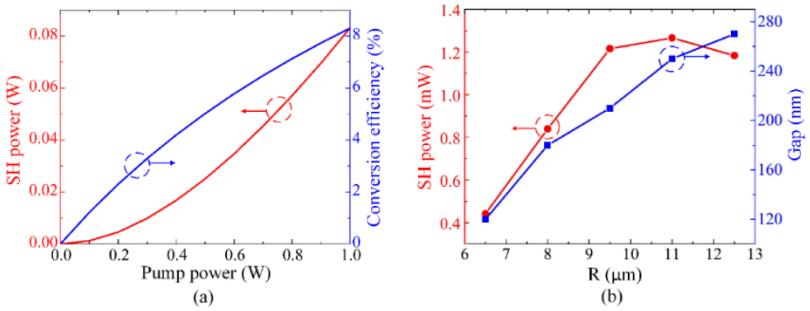

Fig. 11. (a) The output SH power (red line) and SHG conversion efficiency (blue line) versus different pump power. (b) With pump power of 100 mW, the SH power and the corresponding optimized gaps under resonance condition.

4. Sensing and upconversion detection

4.1. Theoretical model and sensor design

Based on the nonlinear upconversion method, we further propose a potential application of this device for on-chip methane gas sensing, as shown in Fig. 12(a). The sensor contains two parts. In the first section, the waveguide with narrower width is covered by a gas chamber which can

be fabricated by PDMS [23]. The MIR light interacts with gas through the evanescent fields of the waveguide modes. In the second section, the MIR light after absorption is injected into the MRR for MIR-to-NIR SHG. There is a taper region between the two sections so as to avoid excess loss. According to the Beer-Lambert Law, the relationship between the output power P_1 after gas absorption and the input power P_0 can be defined as [35]

$$P_1 = P_0 \exp(-\varepsilon \Gamma C L_1 - \alpha_{prop} L_1) \tag{11}$$

where ε is the molar absorption, C is the methane concentration, α_{prop} is the propagation loss of the first waveguide, and Γ is the evanescent power factor defined as [17]

$$\Gamma = \frac{\iint_{gas} P_z \, dxdy}{\iint_{total} P_z \, dxdy} \tag{12}$$

where P_z is the z component of the Poynting vector normal to the waveguide cross section. The evanescent power factor Γ, which indicates the overlap of the interactions between the gas and the mode field, has a significant influence on the sensing performance.

The output power P_1 of the first waveguide is the pump power of the MRR. Through the SHG process in the MRR, the output SH power P_2 is detected by the NIR detector. The minimum concentration measured by the sensor indicates the DL, which is determined by the minimum detectable power $P_{min} = P_2$ (C = 0) - P_2 ($C = C_{min}$), where P_2 (C = 0) is the output power for a null concentration and P_2 ($C = C_{min}$) is the output power for the minimum concentration [18]. In practice, P_{min} is determined by the resolution of the NIR detector, which can be as low as 1×10^{-12} W. In this case, the minimum detectable concentrations C_{min} can be estimated as follows, firstly, the light-gas interaction in the first waveguide causes a variation in the pump power for SHG in the MRR, and then the NIR detector will detect a variation at the output. By assuming the variation of the output power caused by gas absorption equal to the NIR detector resolution, the minimum concentration can be obtained by solving the coupled mode equations in MRR to match such variation.

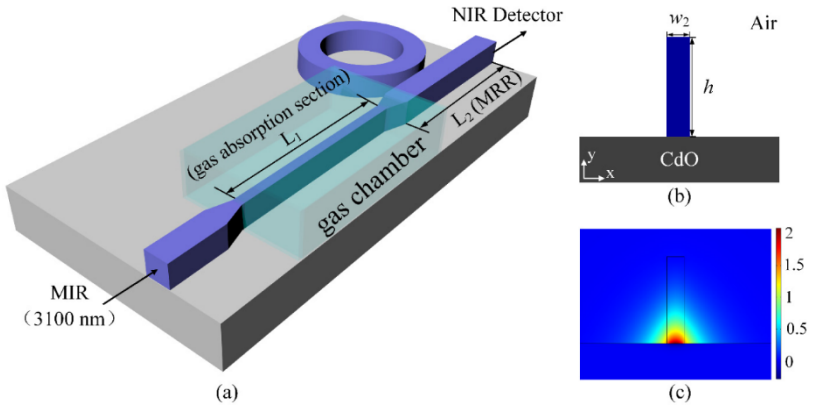

Fig. 12. (a) The schematic of gas sensing. (b) The structure of the first waveguide, and (c) mode profile at FF, when the first waveguide width w_2 = 400 nm.

As mentioned above, the gas absorption occurs in the first waveguide, thus it is important to ensure large evanescent fields in this section. As shown in Fig. 12(b), we choose the first waveguide width w_2 = 400 nm to ensure large phase mismatch between FF and SHF, and the mode profile at FF is demonstrated in Fig. 12(c). In this condition, the evanescent power factor Γ = 69% and propagation loss α_{prop} = 0.0782 dB·μm^{-1}. With narrow waveguide, the scattering loss induced by the sidewall roughness can have effect on the total loss. At NIR wavelength, the

Optics EXPRESS

typical scattering losses of the polymer waveguide can be kept within ~1 dB·cm^{-1} [36]. At longer wavelength e.g. 3100 nm, a stronger resistance to sidewall roughness can be expected [37]. Furthermore, it is known that the scattering loss induced by the sidewall roughness has stronger impact on TE mode, while in our design, the TM mode is employed for sensing. Finally, we would like to emphasize that, in the plasmonic waveguide, the main contribution of loss is from the absorption of metal or metal-like materials, e.g. CdO in the proposed waveguide. With waveguide width of 400 nm, the TM mode loss at 3100 nm caused by the CdO substrate is ~782 dB·cm^{-1}, almost two orders of typical scattering loss. Therefore, the total loss is dominated by the material absorption.

4.2. Performance analysis

With R and g of the MRR fixed to 11 μm and 250 nm, the variations of the DL with the first waveguide length L_1 at different input pump powers are demonstrated in Fig. 13(a). For the input pump power P_0 = 100 mW, the DL initially decreases as the waveguide length increases, reaching a minimum value of 1.45 nmol/L at L_1 = 30 μm and then rises. The DL reaches a minimum at L_1 = 30 μm with different pump powers. We define the waveguide length corresponding to the minimum DL as the optimal length (L_{opt}). Moreover, the DL decreases as the pump power increases. For the pump power P_0 = 400 mW, the DL reaches 0.106 nmol/L at L_{opt} = 30 μm. In addition, as the pump power increases, the DL varies little with the first waveguide length. Therefore, this structure has a larger fabrication tolerance at a higher pump power. As shown in Fig. 13(b), the DL variation is quite small at the optimal length L_{opt} = 30 μm when the pump power ranging from 0.4 W to 1 W. Therefore, one cannot always use higher pump power to enhance the DL.

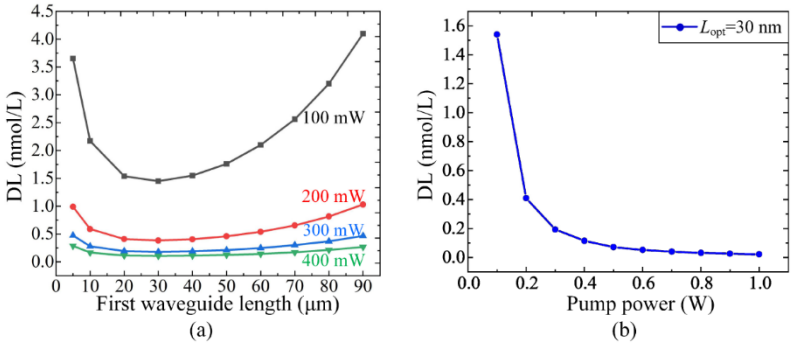

Fig. 13. (a) The variations of the DL with the first waveguide length under different input pump power. (b) The DL with respect to different pump power at L_{opt} = 30 μm.

With optimal length L_{opt} = 30 μm and the input pump power P_0 = 100 mW, we further compare the sensing performances of the proposed cascaded sensing scheme and the MIR direct detection. The normalized power defined as $P = P(C)/P(C = 0)$ varies with different methane concentrations is shown in Fig. 14. It can be seen that as the methane concentration increases, the normalized power decreases more significantly in the NIR upconversion detection scheme than in the MIR direct detection scheme.

Optics EXPRESS

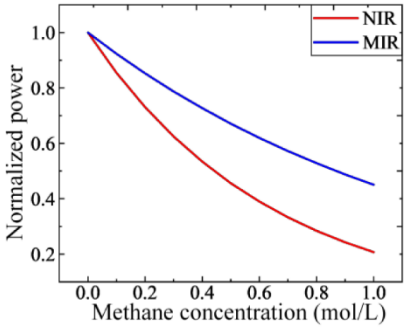

Fig. 14. The normalized power (P(C)/P(C = 0)) with respect to different methane concentration in the NIR upconversion detection scheme (red line) and the MIR direct detection scheme (blue line).

In order to study the influence of the first waveguide width w_2 on the sensing performance, we fix to the structure parameters of the MRR (g = 250 nm and R = 11 μm) and the input pump power P_0 = 100 mW, respectively. The waveguide propagation loss is important for sensor sensitivity [17]. The propagation loss α_{prop} and the optimal length of the first waveguide L_{opt} at different width as show in Fig. 15(a). The narrower the first waveguide width, the smaller the propagation loss and the longer corresponding optimal length can be obtained. On the contrary, a large propagation loss results in a short optimal length and consequently limiting the DL. Therefore, the relationship between propagation loss and gas absorption is competitive. Figure 15(b) depicts the variation of the evanescent power factor as a function of the first waveguide width. It can be seen that the evanescent power factor can reach about 80% at w_2 = 300 nm, in this condition, the corresponding DL can achieve 1.04 nmol/L at L_{opt} = 34 μm, as shown in Fig. 15(c). Moreover, the larger the evanescent power factor, the smaller the DL obtained.

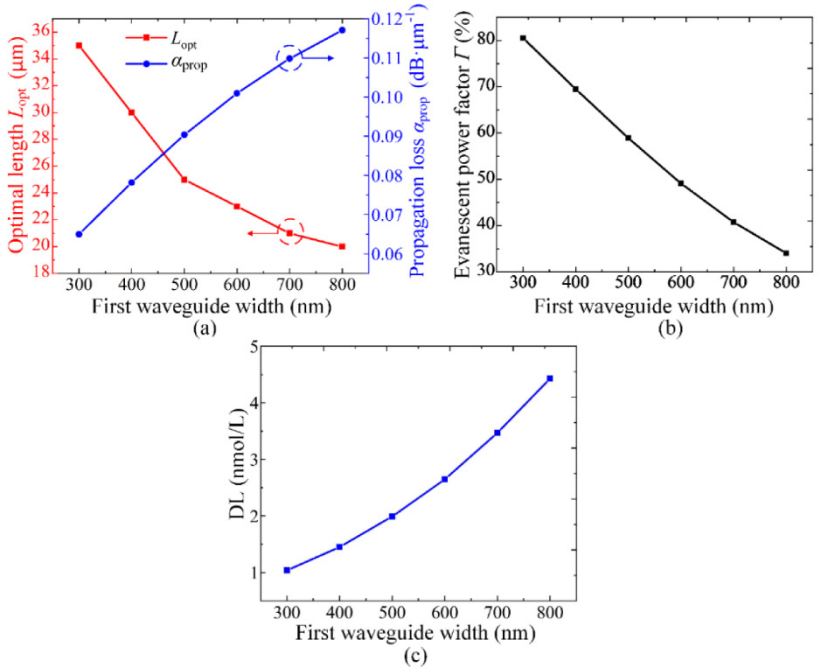

Fig. 15. (a) Optimal length L_{opt} and propagation loss α_{prop}, (b) the evanescent power factor Γ, and (c) the DL at the optimal length with respect to different first waveguide width.

Optics EXPRESS

Next, with the first waveguide length and width fixed to 34 μm and 300 nm, we investigate the impact of the gap of MRR on the DL with 100 mW pump power, as shown in Fig. 16. It can be seen that the DL first drops to the minimum value of 1.04 nmol/L at g = 250 nm and then rises. The DL of 1.04 nmol/L in the proposed device is nearly two orders of magnitude lower than the one obtained in the subwavelength grating waveguide [38] and the ridge waveguide based on chalcogenide glasses [18], and almost four orders of magnitude lower than the one obtained in the Ge-rich SiGe waveguides [39]. This optimal gap size corresponds to the maximum SHG conversion efficiency as well. Therefore, higher SHG efficiency can enhance the power variation caused by methane absorption, so that lower methane concentrations can be detected. However, the overall DL variation with different gap size is not pronounced indicating robust tolerance on this parameter.

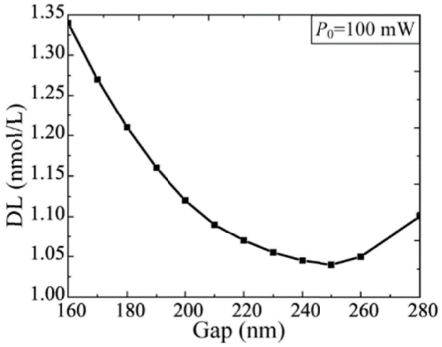

Fig. 16. The DL with respect to different gaps of the MRR with pump power P_0 = 100 mW.

5. Conclusion

In summary, we theoretically propose a bicharacteristic waveguide for SHG from MIR to NIR. Leveraging the unique dispersion relation of CdO, the PMC for SHG can be satisfied between the fundamental plasmonic mode at FF and photonic mode at SHF, respectively. The SH conversion efficiency of 4.173% can be obtained with waveguide length of 90.3 μm under 1 W pump power. To further enhance the conversion efficiency, a MRR is designed and optimized based on the proposed waveguide. It is shown that the required pump power can be much lower compare to the straight waveguide and SHG conversion up to 1.27% can be obtained even with the existence of bending loss. Furthermore, we propose a cascaded configuration for simultaneous MIR gas sensing and frequency upconversion based on such waveguide. The DL dependence on various parameters are investigated and analyzed in detail. The results show that the DL of 1.04 nmol/L can be obtained with proper waveguide dimension and input power. The cascaded structure provides a promising candidate for high-performance gas sensing.

Funding

Wuhan Science and Technology Bureau (2018010401011297); National Natural Science Foundation of China (61605179); Fund of Hubei Key Laboratory of Inland Shipping Technology (NHHY2018002); Fundamental Research Funds for the Central Universities, China University of Geosciences (Wuhan) (162301132703, G1323511794, and CUG2018JM16); Experimental Technology Research Funds (SJ-201816); China University of Geosciences (Wuhan) Teaching Laboratory Open Funds (SKJ2018131).

References

1. C. Langrock, S. Kumar, J. E. McGeehan, A. Willner, and M. Fejer, "All-optical signal processing using $\chi^{(2)}$ nonlinearities in guided-wave devices," J. Lightwave Technol. **24**(7), 2579–2592 (2006).
2. S. Zlatanovic, J. S. Park, S. Moro, J. M. C. Boggio, I. B. Divliansky, N. Alic, S. Mookherjea, and S. Radic, "Mid-infrared wavelength conversion in silicon waveguides using ultracompact telecom-band-derived pump source," Nat. Photonics **4**(8), 561–564 (2010).

Optics EXPRESS

3. S. Farazi and A. Zarifkar, "A low-power optical nanoswitch based on XPM-enhanced second harmonic generation," J. Lightwave Technol. **35**(10), 1988–1994 (2017).
4. M. Cazzanelli, F. Bianco, E. Borga, G. Pucker, M. Ghulinyan, E. Degoli, E. Luppi, V. Véniard, S. Ossicini, D. Modotto, S. Wabnitz, R. Pierobon, and L. Pavesi, "Second-harmonic generation in silicon waveguides strained by silicon nitride," Nat. Mater. **11**(2), 148–154 (2012).
5. M. Kauranen and A. V. Zayats, "Nonlinear plasmonics," Nat. Photonics **6**(11), 737–748 (2012).
6. W. H. P. Pernice, C. Xiong, C. Schuck, and H. X. Tang, "Second harmonic generation in phase matched aluminum nitride waveguides and micro-ring resonators," Appl. Phys. Lett. **100**(22), 223501 (2012).
7. F. F. Lu, T. Li, X. P. Hu, Q. Q. Cheng, S. N. Zhu, and Y. Y. Zhu, "Efficient second-harmonic generation in nonlinear plasmonic waveguide," Opt. Lett. **36**(17), 3371–3373 (2011).
8. B. N. Carnio and A. Y. Elezzabi, "Second harmonic generation in metal-$LiNbO_3$-metal and $LiNbO_3$ hybrid-plasmonic waveguides," Opt. Express **26**(20), 26283–26291 (2018).
9. J. Zhang, E. Cassan, D. Gao, and X. Zhang, "Highly efficient phase-matched second harmonic generation using an asymmetric plasmonic slot waveguide configuration in hybrid polymer-silicon photonics," Opt. Express **21**(12), 14876–14887 (2013).
10. T. Huang, P. M. Tagne, and S. Fu, "Efficient second harmonic generation in internal asymmetric plasmonic slot waveguide," Opt. Express **24**(9), 9706–9714 (2016).
11. S. V. Rao, K. Moutzouris, and M. Ebrahimzadeh, "Nonlinear frequency conversion in semiconductor optical waveguides using birefringent, modal and quasi-phase-matching techniques," J. Opt. A, Pure Appl. Opt. **6**(6), 569–584 (2004).
12. Y. Sun, Z. Zheng, J. Cheng, G. Sun, and G. Qiao, "Highly efficient second harmonic generation in hyperbolic metamaterial slot waveguides with large phase matching tolerance," Opt. Express **23**(5), 6370–6378 (2015).
13. M. Gromovyi, J. Brault, A. Courville, S. Rennesson, F. Semond, G. Feuillet, P. Baldi, P. Boucaud, J. Y. Duboz, and M. P. De Micheli, "Efficient second harmonic generation in low-loss planar GaN waveguides," Opt. Express **25**(19), 23035–23044 (2017).
14. B. Janjan, V. Ahmadi, M. Miri, and D. Fathi, "First-order forward and backward quasi-phase matched second harmonic generation in silicon-organic hybrid structures," J. Lightwave Technol. **36**, 5137–5144 (2018).
15. X. Sun, D. Dai, L. Thylén, and L. Wosinski, "High-sensitivity liquid refractive-index sensor based on a Mach-Zehnder interferometer with a double-slot hybrid plasmonic waveguide," Opt. Express **23**(20), 25688–25699 (2015).
16. B. Kumari, A. Barh, R. K. Varshney, and B. P. Pal, "Silicon-on-nitride slot waveguide: a promising platform as mid-IR trace gas sensor," Sensor. Actuat. Biol. Chem. **236**, 759–764 (2016).
17. B. Kumari, R. K. Varshney, and B. P. Pal, "Design of chip scale silicon rib slot waveguide for sub-ppm detection of N_2O gas at mid-IR Band," Sensor. Actuat. Biol. Chem. **255**, 3409–3416 (2017).
18. A. Gutierrez-Arroyo, E. Baudet, L. Bodiou, V. Nazabal, E. Rinnert, K. Michel, B. Bureau, F. Colas, and J. Charrier, "Theoretical study of an evanescent optical integrated sensor for multipurpose detection of gases and liquids in the mid-infrared," Sensor. Actuat. Biol. Chem. **242**, 842–848 (2017).
19. S. Wolf, T. Trendle, J. Kiessling, J. Herbst, K. Buse, and F. Kühnemann, "Self-gated mid-infrared short pulse upconversion detection for gas sensing," Opt. Express **25**(20), 24459–24468 (2017).
20. L. Høgstedt, J. S. Dam, A. L. Sahlberg, Z. Li, M. Aldén, C. Pedersen, and P. Tidemand-Lichtenberg, "Low-noise mid-IR upconversion detector for improved IR-degenerate four-wave mixing gas sensing," Opt. Lett. **39**(18), 5321–5324 (2014).
21. Y. Yang, K. Kelley, E. Sachet, S. Campione, T. S. Luk, J. P. Maria, M. B. Sinclair, and I. Brener, "Femtosecond optical polarization switching using a cadmium oxide-based perfect absorber," Nat. Photonics **11**(6), 390–395 (2017).
22. T. Huang, J. Pan, Z. Cheng, C. Song, J. Wang, X. Shao, P. P. Shum, and G. Brambilla, "Photon-plasmon coupling for fundamental-mode phase-matched third harmonic and triplet photon generation," J. Lightwave Technol. **36**(18), 3892–3897 (2018).
23. H. W. Lee, G. Papadakis, S. P. Burgos, K. Chander, A. Kriesch, R. Pala, U. Peschel, and H. A. Atwater, "Nanoscale conducting oxide PlasMOStor," Nano Lett. **14**(11), 6463–6468 (2014).
24. I. C. Reines, M. G. Wood, T. S. Luk, D. K. Serkland, and S. Campione, "Compact epsilon-near-zero silicon photonic phase modulators," Opt. Express **26**(17), 21594–21605 (2018).
25. S. Kim and M. Qi, "Broadband second-harmonic phase-matching in dispersion engineered slot waveguides," Opt. Express **24**(2), 773–786 (2016).
26. I. P. Radko, S. I. Bozhevolnyi, G. Brucoli, L. Martin-Moreno, F. J. Garcia-Vidal, and A. Boltasseva, "Efficiency of local surface plasmon polariton excitation on ridge," Phys. Rev. B Condens. Matter Mater. Phys. **78**(11), 115115 (2008).
27. I. P. Radko, S. I. Bozhevolnyi, G. Brucoli, L. Martín-Moreno, F. J. García-Vidal, and A. Boltasseva, "Efficient unidirectional ridge excitation of surface plasmons," Opt. Express **17**(9), 7228–7232 (2009).
28. J. Lu, C. Petre, and E. Yablonovitch, "Numerical optimization of a grating coupler for the efficient excitation of surface plasmons at an Ag-SiO_2 interface," J. Opt. Soc. Am. B **24**(9), 2268–2272 (2007).
29. F. F. Lu, T. Li, J. Xu, Z. D. Xie, L. Li, S. N. Zhu, and Y. Y. Zhu, "Surface plasmon polariton enhanced by optical parametric amplification in nonlinear hybrid waveguide," Opt. Express **19**(4), 2858–2865 (2011).
30. M. E. D. Rosa, W. Su, M. C. Brant, and D. G. Mclean, "Elastic polymer guest-host optical limiters," MRS Online Proc. Libr. **479**, 83 (1997).

Optics EXPRESS

31. X. Y. Zhang, A. Hu, J. Z. Wen, T. Zhang, X.-J. Xue, Y. Zhou, and W. W. Duley, "Numerical analysis of deep sub-wavelength integrated plasmonic devices based on Semiconductor-Insulator-Metal strip waveguides," Opt. Express **18**(18), 18945–18959 (2010).
32. J. Zhang, E. Cassan, and X. Zhang, "Enhanced mid-to-near-infrared second harmonic generation in silicon plasmonic microring resonators with low pump power," Photon. Res. **2**(5), 143–149 (2014).
33. K. Okamoto, *Fundamentals of Optical Waveguides* (Academic, 2010).
34. T. Zhang, X. Yin, L. Chen, and X. Li, "Ultra-compact polarization beam splitter utilizing a graphene-based asymmetrical directional coupler," Opt. Lett. **41**(2), 356–359 (2016).
35. Z. Han, P. Lin, V. Singh, L. Kimerling, J. Hu, K. Richardson, A. Agarwal, and D. T. H. Tan, "On-chip mid-infrared gas detection using chalcogenide glass waveguide," Appl. Phys. Lett. **108**, 141106 (2016).
36. T. Ling, S. L. Chen, and L. J. Guo, "Fabrication and characterization of high Q polymer micro-ring resonator and its application as a sensitive ultrasonic detector," Opt. Express **19**(2), 861–869 (2011).
37. F. Grillot, L. Vivien, S. Laval, and E. Cassan, "Propagation loss in single-mode ultrasmall square silicon-on-insulator optical waveguide," J. Lightwave Technol. **24**(2), 891–896 (2006).
38. A. Gervais, P. Jean, W. Shi, and S. LaRochelle, "Design of slow-light subwavelength grating waveguides for enhanced on-chip methane sensing by absorption spectroscopy," IEEE J. Sel. Top. Quantum Electron. **25**(3), 1–8 (2019).
39. Q. Liu, J. Ramirez, V. Vakarin, X. Roux, A. Ballabio, J. Frigerio, D. Chrastina, G. Isella, D. Bouville, L. Vivien, C. Ramos, and D. Marris-Morini, "Mid-infrared sensing between 5.2 and 6.6 μm wavelengths using Ge-rich SiGe waveguides [Invited]," Opt. Mater. Express **8**(5), 1305–1312 (2018).